This article has been accepted for publication in IEEE Transactions on Energy Conversion. This is the author's version which has not been fully edited and content may change prior to final publication. Citation information: DOI 10.1109/TEC.2024.3375256

Detailed Multi-Domain Modeling and Faster-Than-Real-Time Hardware Emulation of Small Modular Reactor for EMT Studies

Weiran Chen, *Student Member, IEEE,* Venkata Dinavahi, *Fellow, IEEE,* and Ning Lin, *Member, IEEE.*

***Abstract*—Small modular reactors (SMRs) are gaining significant attention as a promising solution to address the global energy demand and simulation is pivotal in expediting the construction of SMRs. However, the point-reactor neutron-kinetics equations of SMRs are strongly stiff nonlinear ordinary differential equations (ODEs), which poses a great difficulty for numerical computation of electromagnetic transients (EMT) of power systems coupled with SMRs. In this paper, a semi-analytical solution is proposed to streamline the comprehensive SMR mathematical model and reduce the model order from 25th to 18th. Additionally, the conglomeration of selected SMR-based EMT power system benchmark, which includes synchronous machines (SMs), modular multilevel converters (MMCs), power distribution networks, and varying loads, is described in detail and implemented on the Xilinx® VCU 118 field-programmable gate array (FPGA) based hardware-in-the-loop (HIL) real-time transient emulation platform. The results demonstrate a significant improvement in computational speed and stability achieved by the proposed solution, which achieves a computational accuracy of IEEE 32-bit single-precision floating-point numbers, with a minimum calculation interval of 800ns, resulting in a remarkable 12.5-fold acceleration in faster-than-real-time (FTRT) performance. This advancement greatly facilitates the simulation of intricate SMR-based models for EMT studies.**

***Index Terms*—Electromagnetic transients (EMT), Faster than real time, Field-programmable gate arrays (FPGAs), Hardware-in-the-loop (HIL), Integral pressurized water reactor (iPWR), Multi-domain co-simulation, Modular multi-level converter (MMC), Real-time systems, Small modular reactor (SMR).**

I. Introduction

NUCLEAR reactors generating below 300MWe are generally classified as SMRs, which have attracted widespread attention due to their modularity, low construction cost, enhanced safety, etc. [1]. Due to the sophisticated design of SMRs, involving nuclear, thermal, mechanical, electrical, hydrodynamic domains, etc., as depicted by the conceptual diagram in Fig. 1, for the purpose of power system analysis by EMT simulations, it is a common practice to build a simplified system-level SMR model with specific focus on particular subsystem which may be modeled in detail [2]–[4].

Differential equations are used to simulate dynamic responses of neutron kinetics with fluctuations at the power grid terminal. Taking the pressurized water reactor (PWR) as an illustration, a 55th-order differential equations mathematical model and its simplified model are discussed in detail, and can be summarized as follows [5]–[13]: (1) *Point-reactor Neutron-kinetics Model*: In order to accurately simulate the physical state of prompt/delayed neutrons within the reactor core, regardless of significant perturbations or critical state, a set of 7th-order ODE model is proposed, incorporating 6 groups of delayed neutrons and a 1st-order prompt neutron component. (2) *Reactor Thermal-hydraulics*: To represent the thermodynamics of the reactor core, Mann's model is widely used [9], where one fuel and two coolant nodes will yield a 3rd-order ODE. The paths where the coolant flows in and out are called the hot leg riser and downcomer. These two components are usually treated as first-order lags, which introduces an additional set of 2nd-order ODE. (3) *Steam Generator*: The three-lump steam generator (SG) Model is extensively utilized, which contains three segments: primary coolant, tube metal, and secondary coolant, resulting in a linear 3rd-order mathematical model. (4) *Rods Control*: As exemplified by constant average coolant temperature control, it contains 3 loop control channels, consisting of multiple filters, lead-lag, nonlinear gain, and hysteresis loop, which can be represented by 5th-order ODE. (5) *Turbine-Governor*: The choice of the steam turbine-governor model is relatively flexible, and the control strategy of the governor varies depending on whether the SMR is operated in the grid-connected or islanded microgrid. Therefore, a simplified 5th-order model is used. Consequently, excluding all auxiliary devices such as the plenum model and pressurizer model [14], the core part of the proposed PWR can be represented by a set of system-level 25th-order ODE.

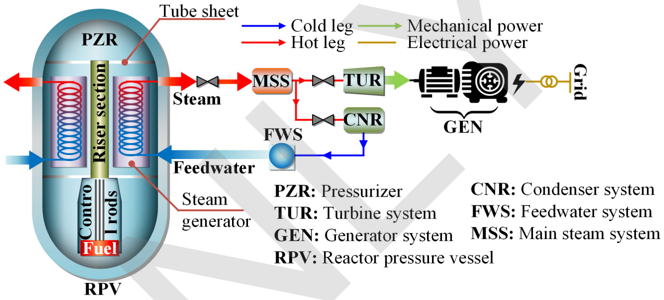

Fig. 1. Sketch of integrated pressurized water reactor (iPWR) [1], [10].

This work was supported in part by the Natural Science and Engineering Research Council of Canada (NSERC). The work of Weiran Chen was supported by the China Scholarship Council (CSC). (Corresponding author: Weiran Chen.) The authors are with the Department of Electrical and Computer Engineering, University of Alberta, Edmonton, Alberta T6G 2V4, Canada. (e-mail: weiran4@ualberta.ca; dinavahi@ualberta.ca; ning3@ualberta.ca).

Such high-order ODEs pose a significant burden on computer calculations, not to mention the coupling with the electrical system simulation that has yet to be considered. Furthermore, the stiff problem of point-reactor neutron-kinetics model presents formidable obstacles. The neutron equations yield an exact solution when some feedbacks are ignored or the reactivity is assumed to be known [15]–[18]. Other attempts have been made to give numerical solutions [19], [20], where the advantage of these methods over traditional explicit numerical solutions, such as Euler and Runge-Kutta, is that their computational time-step h is not limited by the absolute stability interval $|h\lambda_{\max}|$ [21]. While the implicit iterative numerical computation method can solve the stiff problem to some extent, the execution times within each time-step has to be greatly increased, thus reducing the real-time performance. Normally, the duration of transient states of neutron kinetics varies from $1e^{-5}$ to $1e^{-3}$ seconds, necessitating the optimization of the mathematical model and corresponding numerical algorithm to satisfy the real-time execution requirements [22].

Hitherto, the International Atomic Energy Agency (IAEA) has recommended the use of HIL as a valuable alternative for assessing systems' performance and identifying potential issues to ensure the safety and reliability of SMRs and nuclear power plants (NPPs), considering that their online verification and validation (V&V) is normally infeasible [23], [24]. However, most of the existing studies on the SMRs HIL emulation are implemented on CPU-based simulation platforms, which suffer from memory limitations and sequential computations [25]. Simultaneously, even if real-time calculation is achieved by using high-performance CPUs, the excessively long evolution time of nuclear reaction such as heat conduction, xenon poisoning, and samarium poisoning effects, which can last from several minutes to even 60 hours, can result in tediously long simulation time [22]. As a result, the necessity for faster-than-real-time (FTRT) emulation has emerged, as it can effectively accelerate the simulation process and assist in predicting the behavior of models, fault prediction, and scenario analysis [26], [27].

To summarise, for power system analysis and EMT studies, there is a need to put efforts into the following research and development (R&D) requirements:

- A suitable numerical solution for point-reactor neutron-kinetics model that does not lose accuracy while solving the problem of stiffness and has good real-time performance while co-simulating with the power system components. Additionally, this method can also be employed for water-cooled nuclear reactors modeling.
- Development and application of a high-performance FTRT HIL emulation platform for detailed SMR models considering reactivity, temperature, rods control and EMT studies.

The main focus of this paper is on developing a detailed 25th-order iPWR-type SMR suitable for FTRT HIL emulation. A semi-analytical solution capable of addressing stiff problems is proposed on neutron equations, successfully achieving a reduction of the order to 18 for the SMR. Furthermore, the utilization of task-level parallelism, hardware pipelining, and breaking data dependencies methods are conducted to realize FTRT computation with an 800ns interval. For validation the real-time performance of the proposed numerical method, a conceptional, open-access real-time 12kV medium-voltage direct current (MVDC) shipboard power system (SPS) emulation benchmark is selected and modified to integrate with the proposed SMR model [28], [29]. The entire system is then implemented on the Xilinx® Virtex UltraScale+ VCU118 FPGA board.

The structure of the rest sections in this paper is as follows: Section II introduces the proposed SMR model and solutions. In Section III, the configuration of the electrical part and the mathematical interface with SMR are presented. Section IV illustrates the time sequence and latency analysis of proposed algorithm, and hardware implementation of the emulator. Finally, real-time emulation results are shown in Section V, and Section VI exhibits the conclusion.

II. Modeling and Optimization of the SMR Model

In this section, a detailed 150MWth/45MWe nonlinear 25th-order mathematical iPWR-type SMR with the semi-analytical solution is presented. The main focus of optimization and acceleration will be on the point-reactor neutron-kinetics model of the previous work [30].

A. *Stiffness Analysis of Point-reactor Neutron-kinetics Model*

When the external neutron source of the nuclear reactor is not considered, the six groups of delayed neutrons point-reactor neutron-kinetics equations are defined as follows:

$$\frac{dn\left(t\right)}{dt}=\frac{\rho\left(t\right)-\beta}{\mathit{\Lambda}}n\left(t\right)+\sum_{i=1}^{6}\lambda_iC_i\left(t\right),\tag{1}$$

$$\frac{dC_i\left(t\right)}{dt}=\frac{\beta_i}{\mathit{\Lambda}}n\left(t\right)-\lambda_iC_i\left(t\right),\tag{2}$$

where $n(t)$ is the mean prompt neutron density; $C_i(t)$ is the delayed neutron density of the ith group; $\rho(t)$ is the core reactivity; $\mathit{\Lambda}$ is the prompt neutron lifetime; β_i is the delayed neutron fraction of the ith group, $\beta=\sum_i\beta_i$; λ_i is the decay constant. When $t\geq 0$, to facilitate analysis, $\rho(t)$ is temporarily replaced by a constant ρ_0. Then, the Laplace transform of $n(t)$ can be derived:

$$N\left(s\right)=\frac{\mathit{\Lambda}\left[n\left(0\right)+\sum_i\frac{\lambda_iC_i(0)}{s+\lambda_i}\right]}{\mathit{\Lambda}s+\beta-\rho_0-\sum_i\frac{\beta_i\lambda_i}{s+\lambda_i}}.\tag{3}$$

Its inverse transformation leads to the general solution:

$$n\left(t\right)=\mathscr{L}^{-1}\left[N\left(s\right)\right]=\sum_{j=1}^{m+1}A_je^{\omega_jt},\tag{4}$$

where m is the number of delayed neutrons groups, A is a constant, and ω is both the eigenvalue of the Jacobian and the root of the denominator of (3), i.e., ω satisfies the following equation:

$$\rho_0=\mathit{\Lambda}\omega+\sum_i\frac{\beta_i\omega}{\omega+\lambda_i}.\tag{5}$$

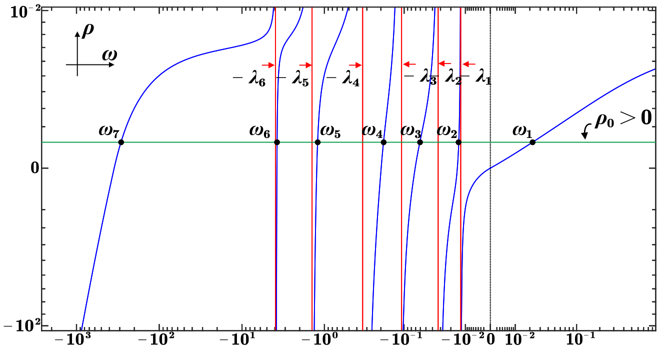

Fig. 2. Graphic solution of six groups of delayed neutron reactivity equation.

Accordingly, the calculated parameters are given as follows: $\Lambda = 2 \times 10^{-5} s$, $\beta_{1\sim 6} = 0.000266$, 0.001491, 0.001316, 0.002849, 0.000896, and 0.000182, respectively; $\lambda_{1\sim 6} = 0.0127 s^{-1}$, $0.0317 s^{-1}$, $0.115 s^{-1}$, $0.311 s^{-1}$, $1.4 s^{-1}$, and $3.87 s^{-1}$, respectively. Then the relationship between ω and $\rho(t)$ can be obtained by the graphical method, see Fig. 2. It can be seen that when $\rho_0 > 0$, (5) has only one positive root ω_1 and the rest are negative roots. At this time, the reactor characteristics will be determined by the ω_1 term, and the rest decay with time. When $\rho_0 < 0$, it is obvious that all the roots of (5) will be negative, and the characteristics of the reactor at this time are determined by the slowest decaying term. Subsequently, according to Fig. 2, the relationship between ω_j, ρ_0, and Λ can be summarized as follows:

$$\omega_1 > -\lambda_1 > \omega_2 > -\lambda_2 > ... > \omega_6 > -\lambda_6 > \omega_7 > -\Lambda^{-1}. \tag{6}$$

Based on the aforementioned analysis, when there are no unstable solutions, i.e., none of the real parts of eigenvalues are large and positive $Rew_j > 0$, the stiffness ratio of (4) $r = \frac{\max|\mathrm{Re}\omega_j|}{\min|\mathrm{Re}\omega_j|} \gg 1$ and its solution is determined by the most negative real part of w_j. In addition, from (6) and Fig. 2, it can be seen that w_j have different orders of magnitude. For further clarification, (1) and (2) can be represented in matrix form:

$$\begin{cases} \dot{\boldsymbol{Y}}(t) = \boldsymbol{F}(t)\boldsymbol{Y}(t) \\ \boldsymbol{Y}(t)|_{t=0} = \boldsymbol{Y}_0 \end{cases}, \tag{7}$$

$$\boldsymbol{F}(t) = \begin{bmatrix} \frac{\rho(t)-\beta}{\Lambda} & \lambda_1 & ... & \lambda_6 \\ \frac{\beta_1}{\Lambda} & -\lambda_1 & 0 & 0 \\ ... & 0 & ... & 0 \\ \frac{\beta_6}{\Lambda} & 0 & 0 & -\lambda_6 \end{bmatrix}, \tag{8}$$

where $\boldsymbol{Y}(t) = [n(t), C_1(t), ..., C_6(t)]^T$, $\boldsymbol{F}(t)$ is a time-varying coefficient matrix, and the initial value $\boldsymbol{Y}_0 = [n_0, C_{1\_0}, ..., C_{6\_0}]^T$. Assuming that $\rho(t)$ is known, for example, a step or ramp function, it can be seen through (8) that $\boldsymbol{F}(t)$ is an ill-conditioned matrix, which further shows that (7) is a strongly stiff equation. The stiff problem poses a challenge to the conventional method of numerical integration. Taking the explicit Euler method as an example, due to the huge difference in the order of magnitude of the eigenvalues and limited to the stability requirement of the solution, the maximum size of time-step $h = (t_{n+1} - t_n)$ of the numerical computation must satisfy: $h < \frac{2}{\max|\omega_i|}$, i.e., h is determined by $\max|\omega_i|$, not $\min|\omega_i|$. This results in a large waste of computational resources and a large accumulation of rounding errors. While implicit algorithms can address stiff problems, their iterative nature tends to slow down the computational speed, making it challenging to meet real-time and FTRT requirements. This aspect will be validated in Section II-C.

B. First-order Taylor Polynomial Numerical Integration Method and Algorithm Validation

In this part, the one time-step interval numerical solution based on first-order Taylor polynomial of (1) and (2) will be presented. Substituting (2) into (1) and integrating along the interval $[t_n, t_{n+1}]$ yields:

$$\begin{aligned} n(t_{n+1}) - n(t_n) = \int \frac{\rho(\tau)}{\Lambda} n(\tau) d\tau - \\ \sum_{i=1}^{6} (C_i(t_{n+1}) - C_i(t_n)). \end{aligned} \tag{9}$$

Performing Taylor's expansion for $n(\tau)$ at t_{n+1} yields:

$$n(\tau) = n(t_{n+1}) + n^{'}(t_{n+1})(\tau - t_{n+1}). \tag{10}$$

By combining (1), (9), and (10), the following equation can be derived:

$$\begin{aligned} & n(t_{n+1}) - n(t_n) = n(t_{n+1}) \int \frac{\rho(\tau)}{\Lambda} d\tau + \\ & n^{'}(t_{n+1}) \int \frac{\rho(\tau)}{\Lambda}(\tau - t_{n+1}) d\tau - \sum_{i=1}^{6} (C_i(t_{n+1}) - C_i(t_n)), \end{aligned} \tag{11}$$

where the expression of $\rho(\tau)$ is a linear combination of the SMR rod control reactivity and temperature feedback:

$$\rho(t) = \beta\rho_{ext}(t) + \alpha_F \Delta T_f(t) + \alpha_C \frac{(\Delta T_{c1}(t) + \Delta T_{c2}(t))}{2}, \tag{12}$$

where $\rho_{ext}(t)$ is the reactivity change induced by control rod, α_F and α_C is the reactivity coefficient of fuel and coolant, respectively, $\Delta T_f(t)$, $\Delta T_{c1}(t)$, and $\Delta T_{c2}(t)$ is the temperature deviation of fuel, coolant node 1, and coolant node 2, respectively. Then, utilizing the trapezium integration to simplify the integral term with $\rho(\tau)$ yields:

$$\begin{cases} F_1 = \int_{t_n}^{t_{n+1}} \frac{\rho(\tau)}{\Lambda} d\tau = \frac{h[\rho(t_{n+1}) + \rho(t_n)]}{2\Lambda} \\ F_2 = \int_{t_n}^{t_{n+1}} \frac{\rho(\tau)}{\Lambda}(\tau - t_{n+1}) d\tau = -\frac{h^2 \rho(t_n)}{2\Lambda} \end{cases}. \tag{13}$$

Now the analytical expression for $C_i(t_{n+1})$ can be obtained by (2):

$$C_i(t_{n+1}) = e^{-\lambda_i h}\left[C_i(t_n) + \frac{\beta_i}{\Lambda} \int n(\tau) e^{(\lambda_i(\tau - t_n))} d\tau\right], \tag{14}$$

and then, substituting (10) into (14) yields:

$$\begin{aligned} C_i(t_{n+1}) = & e^{-\lambda_i h} C_i(t_n) + \\ & \frac{\beta_i}{\Lambda}\left[G_{1,i} n(t_{n+1}) + G_{2,i} n^{'}(t_{n+1})\right], \end{aligned} \tag{15}$$

$$G_{1,i} = e^{(-\lambda_i h)} \int_{t_n}^{t_{n+1}} e^{(\lambda_i(\tau - t_n))} d\tau = e^{(-\lambda_i h)} \frac{e^{\lambda_i h} - 1}{\lambda_i}, \tag{16}$$

$$\begin{aligned} G_{2,i} &= e^{(-\lambda_i h)} \int_{t_n}^{t_{n+1}} (\tau - t_{n+1})\, e^{(\lambda_i(\tau - t_n))} d\tau \\ &= e^{(-\lambda_i h)} \frac{1 - e^{\lambda_i h} + \lambda_i h}{\lambda_i^2}. \end{aligned} \tag{17}$$

Combining (1) and (15∼17), the expression (18) for $n^{'}(t_{n+1})$ in terms of $n(t_{n+1})$ can be obtained. Following that, combining (1), (15∼17), and (18), the expression for $n(t_{n+1})$ can be derived in (19), while completing the order reduction (7th-order ODE) of the SMR model and the sequential flowchart for SMR solving is depicted in Fig. 3, where $\boldsymbol{X}(t)$, $\boldsymbol{U}(t)$, $\boldsymbol{A}$, and $\boldsymbol{B}$ represent the state space form of the SMR mathematical model, denoting the state variables, inputs, and coefficient matrices, respectively. A detailed explanation will be provided in Section II-D.

However, it can be seen that the solution of $n(t_{n+1})$ is not instantly feasible since these variables are solved in conjunction with other ODEs, particularly with regard to the term $\rho(t)$. Therefore, the unit delay $\rho(t) = z^{-1} *$ (12) is introduced, which enables the solutions for $n(t_{n+1})$ and $n^{'}(t_{n+1})$ to be obtained within one time step. Although z^{-1} can lead to errors, it is insignificant when the ratio between the system's inertia and h is sufficiently large. In typical scenarios, the duration of transient states caused by $\rho(t)$ is usually on the order of minutes [22]. Therefore, taking an example where $h = 0.1s$ and the transient time duration is one minute, the ratio between them can be as high as 600 times. The disparity is significant, making errors caused by unit delay negligible.

The local truncation error (LTE) of $n(t_{n+1})$ is $\frac{n^{(r+1)}(t_{n+1})}{(r+1)^!} h^{(r+1)}$, where r is the $r_{th}-$order Taylor approximation. Admittedly, increasing the order of the Taylor expansion can improve the precision. Nevertheless, higher-order derivatives are frequently challenging [20]. With a second-order Taylor expansion, $\rho'(t)$ is involved. Considering (12), it is evident that taking the derivative of $\rho(t)$ involves the derivatives of multiple variables, significantly increasing the complexity of the formula. Consequently, when considering temperature and reactivity feedback, higher-order Taylor expansions are not recommended.

C. Experimental Validation and Performance Comparison

Based on the parameters mentioned in Section II-A, the changes of $n(t)$ in per-unit will be tested under three scenarios of $\rho(t)$: step inputs 0.003, -0.007, and 0.007, as presented in Table I and the relative error is illustrated in Fig. 4. The compared algorithms selected were ODE solvers of Matlab®: ode4 and ode15s, which are based on the Runge-Kutta explicit integration algorithm and Numerical differentiation formulas (NDFs), respectively [31]. Since ode15s is designed to solve stiff problems with a variable time-step ($h \leq 10\mu s$), its computational results were considered as reference. As for the implicit method, this paper opted for a comparison with the Hammer-Hollingsworth Implicit Runge-Kutta method (IRK) based on Jacobi iteration [32].

When $\rho(t)$ is negative or relatively small ($\rho(t) \ll \beta$), it is referred to as the delayed critical, during which $C_i(t)$ exert a significant influence on the core, rendering it essentially stiff. At this point, the computational results of the RK4 fail to converge, whereas the IRK and the proposed method exhibit good convergence, achieving accuracies of 4% and 0.01%, respectively. The introduced analytical solution in our method contributes to its enhanced precision.

When $\rho(t) = \beta$ or $\rho(t) > \beta$, they are respectively referred to as prompt critical and prompt supercritical. During these conditions, $C_i(t)$ almost becomes ineffective, and the equation's stiffness is significantly reduced. From a numerical computation perspective, LTE becomes the primary concern. It can be observed that, the results of the RK have already converged, and their accuracy is superior to that of our proposed method as well as the IRK. In terms of accuracy order, our method does not exhibit an advantage compared to high-order accuracy numerical methods. However, the errors remain acceptable ($< 1\%$). If h is reduced to 0.01, the calculation accuracy of the proposed method can be greatly improved.

The subsequent analysis involves a quantitative assessment of computational speed, with the latency and resource consumption obtained through Vitis High-Level-Synthesis® (HLS) tool for the three algorithms presented in the Table I below, where DSP, FF, and LUT represent digital signal processor, flip-flop, and lookup table, respectively. For RK4, its latency is 488, calculated at a rate of $10ns$ per latency, its fastest achievable real-time calculation step size is approximately $5\mu s$. For IRK, with a maximum set iteration count of 50, its fastest real-time latency ranges from $8.4\mu s$ to $0.1412ms$. In contrast, the proposed method can achieve a real-time latency as fast as $0.8\mu s$. The main reason for such differences lies in the strong data dependency of RK's computational method, and IRK's dependence on Jacobi iteration. Although both methods have advantages in solving LTE, they are clearly inferior to the proposed method in terms of computational

$$n^{'}(t_{n+1}) = \frac{\left(\frac{\rho(t_{n+1}) - \beta}{\mathit{\Lambda}} + \sum_{i=1}^{6} \frac{\lambda_i \beta_i}{\mathit{\Lambda}} G_{1,i}\right) n(t_{n+1}) + \sum_{i=1}^{6} \lambda_i e^{-\lambda_i h} C_i(t_n)}{\left(1 - \sum_{i=1}^{6} \frac{\lambda_i \beta_i}{\mathit{\Lambda}} G_{2,i}\right)}. \tag{18}$$

$$n(t_{n+1}) = \frac{n(t_n) + \sum_{i=1}^{6} C_i(t_n) - \sum_{i=1}^{6} e^{(-\lambda_i h)} C_i(t_n) + \frac{\left(F_2 - \sum_{i=1}^{6} \frac{\beta_i}{\mathit{\Lambda}} G_{2,i}\right)\left(\sum_{i=1}^{6} \lambda_i e^{(-\lambda_i h)} C_i(t_n)\right)}{\left(1 - \sum_{i=1}^{6} \frac{\lambda_i \beta_i}{\mathit{\Lambda}} G_{2,i}\right)}}{1 - F_1 + \sum_{i=1}^{6} \frac{\beta_i}{\mathit{\Lambda}} G_{1,i} - \left(F_2 - \sum_{i=1}^{6} \frac{\beta_i}{\mathit{\Lambda}} G_{2,i}\right)\left(\frac{\rho(t_{n+1}) - \beta}{\mathit{\Lambda}} + \sum_{i}^{6} \frac{\lambda_i \beta_i}{\mathit{\Lambda}} G_{1,i}\right) / \left(1 - \sum_{i=1}^{6} \frac{\lambda_i \beta_i}{\mathit{\Lambda}} G_{2,i}\right)}. \tag{19}$$

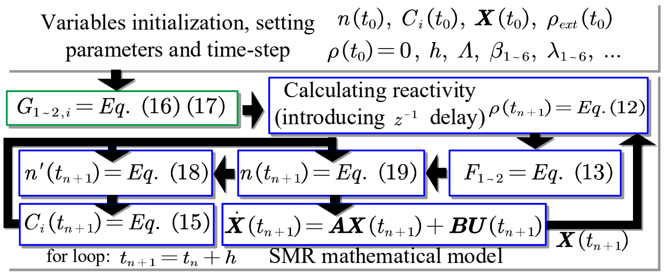
Variables initialization, setting parameters and time-step
$n(t_0),\ C_i(t_0),\ \boldsymbol{X}(t_0),\ \rho_{ext}(t_0)$
$\rho(t_0)=0,\ h,\ \Lambda,\ \beta_{1\sim6},\ \lambda_{1\sim6},\ \dots$
$G_{1\sim2,i}=Eq.\ (16)\ (17)$
Calculating reactivity (introducing z^{-1} delay)
$\rho(t_{n+1})=Eq.\ (12)$
$n'(t_{n+1})=Eq.\ (18)$
$n(t_{n+1})=Eq.\ (19)$
$F_{1\sim2}=Eq.\ (13)$
$C_i(t_{n+1})=Eq.\ (15)$
$\dot{\boldsymbol{X}}(t_{n+1})=\boldsymbol{AX}(t_{n+1})+\boldsymbol{BU}(t_{n+1})$
$\boldsymbol{X}(t_{n+1})$
for loop: $t_{n+1}=t_n+h$
SMR mathematical model

Fig. 3. Flowchart of sequential execution solver for SMR model.

TABLE I
COMPARISON OF ACCURACY AND COMPUTATIONAL SPEED ACROSS DIFFERENT ALGORITHMS

The Mean Prompt Neutron Density with Different Step Reactivity $\rho(t)$ at $h=0.1$					
$\boldsymbol{\rho(t)=0.003\ (<\beta)}$	$\boldsymbol{t=0.2s}$	$\boldsymbol{t=0.4s}$	$\boldsymbol{t=0.6s}$	$\boldsymbol{t=0.8s}$	$\boldsymbol{t=1s}$
RK4	∞	∞	∞	∞	∞
IRK	1.62601	1.87942	2.01729	2.11858	2.20795
Proposed method	1.85116	1.94754	2.03789	2.12481	2.20983
Reference	1.85126	1.94759	2.03792	2.12483	2.20984
$\boldsymbol{\rho(t)=-0.007\ (\ll\beta)}$	$\boldsymbol{t=0.2s}$	$\boldsymbol{t=0.4s}$	$\boldsymbol{t=0.6s}$	$\boldsymbol{t=0.8s}$	$\boldsymbol{t=1s}$
RK4	∞	∞	∞	∞	∞
IRK	0.50156	0.48521	0.47131	0.45912	0.44818
Proposed method	0.48098	0.46529	0.45197	0.44027	0.42978
Reference	0.48097	0.46528	0.45196	0.4402	0.42978
$\boldsymbol{\rho(t)=0.007\ (>\beta)}$	$\boldsymbol{t=0.2s}$	$\boldsymbol{t=0.4s}$	$\boldsymbol{t=0.6s}$	$\boldsymbol{t=0.8s}$	$\boldsymbol{t=1s}$
RK4	159.725	1667.28	17131.7	175888	180570
IRK	159.726	1667.29	17131.9	175891	180572
Proposed method	159.425	1659.35	17000.4	174029	178136
Proposed method (h=0.01)	159.723	1667.21	17130.7	175873	180550
Reference	159.752	1667.56	17134.7	175919	180602
Different Algorithm Performances in HLS Design					
Algorithm	**Latency (cycles)**	**DSP**	**FF**	**LUT**	
RK4	488	116	16,995	15,623	
IRK (min iteration)	841	82	17,083	15,515	
IRK (average iteration)	7345	82	17083	15,515	
IRK (max iteration)	14120	82	17,083	15,515	
Proposed method	80	61	5.949	5,686	

speed. The parallel scheme for the proposed method will be discussed in the Section IV.

In summary, when the system is in a delayed critical state and exhibits significant equation stiffness, the proposed method shows advantages in both calculation speed and accuracy. In the prompt critical state, although the accuracy of the proposed method is slightly inferior, it remains within an acceptable range and can be corrected by reducing h without a significant delay. Moreover, it still maintains an absolute advantage in terms of calculation speed. In real-life scenarios, the prompt critical can lead to a rapid explosion of neutrons in a short time, triggering highly dangerous situations that must be strictly avoided [7]. Therefore, in situations where $\rho(t) < \beta$, our method holds considerable practical significance.

D. SMR Multi-Domain Mathematical Model

The 18th-order state space form of SMR model, state space variables, inputs, state space matrices, the expression of $\rho_{ext}(t)$, corresponding interpretation of all elements, key parameters are shown in (20), (21), (22), (23), Fig. 5, Table II, and Table III. Since the comprehensive modeling of SMRs has been extensively discussed in the existing literatures [4], [8], [10], it will not be reiterated here.

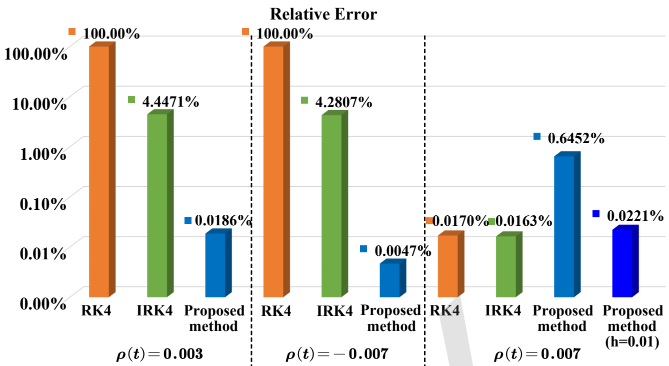

Fig. 4. Different algorithms average relative error with step size $h = 0.1$ compared to Ode15s.

$$\begin{cases} \dot{\boldsymbol{X}}(t) = \boldsymbol{AX}(t) + \boldsymbol{BU}(t) \\ \boldsymbol{X}(t)\left|_{t=0}\right. = \boldsymbol{X}_0 \\ \hat{Y}(t) = \underbrace{[0 \quad \cdots \quad 0}_{Index\ 1_{st}\sim 8_{th}} \quad 1 \quad 1 \quad \underbrace{0 \quad \cdots \quad 0]}_{Index\ 11_{th}\sim 18_{th}} \boldsymbol{X}(t) \end{cases}, \tag{20}$$

$$\boldsymbol{X}(t) = \begin{matrix} [T_f(t) & T_{c1}(t) & T_{c2}(t) & T_{HL}(t) & T_{cin}(t) & T_p(t) \\ T_m(t) & P_s(t) & tb_1(t) & tb_2(t) & tb_3(t) & \tilde{y}(t) \\ y(t) & x_1(t) & x_2(t) & x_3(t) & x_4(t) & x_5(t)]^{\boldsymbol{T}} \end{matrix}, \tag{21}$$

$$\boldsymbol{U}(t) = \begin{bmatrix} n(t) & w(t) & w_{ref} & P_{ref} \end{bmatrix}^T, \tag{22}$$

$$\begin{cases} \tilde{g} = x_5(t) + \dfrac{t_7\left(\frac{n(t)}{N_{0,N}t_1} - x_3(t)\right)}{t_1}, \\ \rho_{ext}(t) = k_{\tilde{\rho}} f_4\left(x_4(t) - x_1(t) - \tilde{g}x_3(t) f_2(x_3(t)) f_3(\tilde{g})\right) \end{cases} \tag{23}$$

where matrices $\boldsymbol{A}$ and $\boldsymbol{B}$ are typical sparse matrices and represented in coordinate format (COO), where a_{ij} and b_{ij} correspond to the elements in the i_{th} row and j_{th} column of $\boldsymbol{A}$ and $\boldsymbol{B}$, respectively, with all unspecified elements set to be 0. $f_{1\sim4}(x)$ are the average coolant temperature & power relation function, variable gain function, nonlinear gain function, and rod speed hysteresis control function, respectively. The detailed explanation of SMR and control system could be found in [30]. The output $\hat{Y}(t)$ of SMR, namely mechanical power $P_m(t) = tb_1(t) + tb_2(t)$, which is input to the SM to generate electricity. In terms of the calculation of $n(t)$, due to introducing the z^{-1} in the control signal $\rho(t)$, according to (19), the value of $n(t_{n+1})$ can be directly calculated based on the initial value and used for iterative calculation of the other ODEs. The motivation behind doing so is to independently separate the solution of the stiff ODEs from the other ODEs, while also downsizing matrices.

III. EMT MODELING OF TWO ZONE MVDC SPS AND INTEGRATION WITH SMR

The offline simulation of the entire model is built on the Simulink®, as illustrated in Fig. 6, while the system's original topology and physical parameters have been followed as closely as possible [29]. This system consists of two zones, including (1) power generation: PGM1: SMRs, SMs, and

TABLE II
STATE SPACE VARIABLES, INPUTS AND ELEMENTS OF SMR AND SM-MMC [30]

State Space Variables, Inputs and Parameters					
$T_f(t)$	Average temperature of fuel	$T_{c1}(t), T_{c2}(t)$	Temperature of coolant in node 1 and 2	$T_{HL}(t), T_{cin}(t)$	Temperature of coolant in hot-leg and cold leg
$T_p(t)$	Temperature of coolant in SG primary loop	$T_m(t)$	Temperature of tube metal lump	$P_s(t)$	Steam pressure
$tb_{1\sim3}(t)$	Turbine state space variables	$\tilde{y}(t)$	Governor droop control variable	$y(t)$	valve position
$x_{1\sim5}(t)$	Constant average coolant temperature control variables	$w(t)$	Synchronous motor speed	w_{ref}, P_{ref}	Motor reference speed and active power
f	Fraction of thermal power in the fuel	P_0	Rated thermal power	$N_{0,N}$	Nominal average neutron density
H	Heat transfer coefficient	A	Effective heat transfer area	m_f, m_c	Mass of fuel and coolant
C_{pf}, C_{pc}	Specific heat of fuel and coolant	$W_{C,N}$	Coolant mass flow rate within the core	τ_{HL}, τ_{CL}	Hot-leg and cold-leg heat transfer time constant
τ_p	Time constant of coolant in SG	τ_m	Time constant of U-type metal tube	τ_{ps}	Time constant of steam pressure
k_{pm}	Temperature coefficient of metal tube	k_{mp}	Temperature coefficient of coolant	k_{pc}, k_{ms}	Temperature coefficient of hot-leg and pressure
k_{psm}, k_{psy}	Pressure coefficient of metal tube and valve	α	Output power coefficient of high-pressure cylinder	τ_{CH}, τ_{RH}	Time constant of high and intermediate reheat steam volume
$t_{1\sim7}$	Time constant of control channel	k_P, k_I	Governor droop control PID parameters	k_{dp}	Droop control gain
$\sigma_{\max}, \sigma_{\min}$	Governor valve opening rate limits	$\mu_{\max}, \mu_{\min}$	Maximum and minimum valve position	$k_{\tilde{\rho}}$	Coefficient of control reactivity variation

Elements of matrices $\boldsymbol{A}_{18\times18}, \boldsymbol{B}_{18\times4}$ (upper) and $\tilde{\boldsymbol{A}}_{13\times13}, \tilde{\boldsymbol{B}}_{13\times3}$ (lower) in COO format : Index Element											
$a_{11} = -a_{12}$	$-\frac{AH}{m_f C_{pf}}$	$a_{21} = a_{31}$	$\frac{AH}{m_c C_{pc}}$	a_{22}	$-\left(\frac{AH}{m_c C_{pc}} + \frac{2W_{C,N}}{m_c}\right)$	$a_{25} = -a_{33}$	$\frac{2W_{C,N}}{m_c}$	a_{32}	$\left(\frac{2W_{C,N}}{m_c} - \frac{AH}{m_c C_{pc}}\right)$	$a_{43} = -a_{44}$	$\frac{1}{\tau_{HL}}$
$a_{54} = a_{55} = \frac{-a_{56}}{2}$	$-\frac{1}{\tau_{CL}}$	a_{64}	$\frac{k_{pc}}{\tau_p}$	$a_{66} = \frac{-a_{67}}{k_{pm}}$	$\frac{-1}{\tau_p}$	$\frac{a_{76}}{k_{mp}} = -a_{77} = \frac{a_{78}}{k_{ms}}$	$\frac{1}{\tau_m}$	$\frac{a_{87}}{k_{psm}} = -a_{88} = \frac{-a_{8,13}}{k_{psy}}$	$\frac{1}{\tau_{ps}}$	a_{98}	$\frac{\alpha y(t)}{\tau_{CH}}$
a_{99}	$\frac{-1}{\tau_{CH}}$	$a_{11,10}$	$\frac{-1}{\tau_{CH}\tau_{RH}}$	$a_{11,11}$	$\frac{-(\tau_{CH}+\tau_{RH})}{\tau_{CH}\tau_{RH}}$	$a_{11,13}$	$\frac{(1-\alpha)P_s(t)}{\tau_{CH}\tau_{RH}}$	$a_{12,12} = \frac{a_{12,13}}{k_I}$	$-k_P$	$a_{13,12}$	$\tilde{y}\left(t\right)\vert_{\sigma_{\min}}^{\sigma_{\max}}$
$a_{14,6}$	$\frac{t_3}{(t_4 t_5)}$	$a_{15,6}$	$\frac{1}{(t_4 t_5)} - \frac{t_3(t_4+t_5)}{(t_4^2 t_5^2)}$	$a_{15,14}$	$\frac{-1}{(t_4 t_5)}$	$a_{15,15}$	$\frac{-(t_4+t_5)}{(t_4 t_5)}$	$a_{16,9} = a_{16,10} = -a_{16,16}$	$\frac{1}{t_6}$	$a_{17,17}$	$\frac{f_1(x_3(t))}{x_4(t)t_2} - \frac{1}{t_2}$
$a_{18,16}$	$\frac{t_7}{t_1^2}$	$a_{18,18}$	$\frac{-1}{t_1}$	b_{11}	$\frac{P_0 f}{N_{0,N} m_f C_{pf}}$	$b_{21} = b_{31}$	$\frac{P_0(1-f)}{N_{0,N} m_f C_{pf}}$	$b_{12,2} = -b_{12,3} = \frac{-b_{12,4}}{k_{dp}}$	$-k_P k_I k_{dp}$	$b_{18,1}$	$\frac{-t_7}{N_{0,N}}$
$\tilde{a}_{11}$	$\frac{-R_a}{L_a}\boldsymbol{I}_{3\times3}$	$\tilde{a}_{13}$	$\frac{-\boldsymbol{M_\Sigma}}{L_a}$	$\tilde{a}_{14}$	$\frac{-\boldsymbol{M_\Delta}}{L_a}$	$\tilde{a}_{15} = \tilde{a}_{16}$	$\mathbb{C}\left[\,\frac{-1}{2L_a}\frac{-1}{2L_a}\frac{-1}{2L_a}\,\right]^T$	$\tilde{a}_{22}$	$\frac{-\left(R_s+\frac{R_a}{2}\right)}{-\left(L_s+\frac{L_a}{2}\right)}\boldsymbol{I}_{2\times2}$	$\tilde{a}_{23}$	$\frac{-2\mathring{\boldsymbol{M}}_{\boldsymbol{\Delta}}}{L_a+2L_s}$
$\tilde{a}_{24}$	$\frac{-2\mathring{\boldsymbol{M}}_{\boldsymbol{\Sigma}}}{L_a+2L_s}$	$\tilde{a}_{31}$	$\frac{n_s\boldsymbol{M_\Sigma}}{\tilde{c}}$	$\tilde{a}_{32}$	$\frac{n_s\bar{\boldsymbol{M}}_{\boldsymbol{\Delta}}}{2\tilde{c}}$	$\tilde{a}_{41}$	$\frac{n_s\boldsymbol{M_\Delta}}{\tilde{c}}$	$\tilde{a}_{42}$	$\frac{n_s\mathring{\boldsymbol{M}}_{\boldsymbol{\Sigma}}}{2\tilde{c}}$	$\tilde{a}_{51} = \tilde{a}_{61}$	$\left[\,\frac{1}{C}\frac{1}{C}\frac{1}{C}\,\right]\mathbb{C}^{-1}$
$\tilde{b}_{22}$	$\begin{bmatrix}\frac{-2R}{L_a+2L_s}\\ 0\end{bmatrix}$	$\tilde{b}_{23}$	$\begin{bmatrix}0\\ \frac{-2R}{L_a+2L_s}\end{bmatrix}$	$\tilde{b}_{51} = \tilde{b}_{61}$	$\frac{1}{C}$						

TABLE III
SUMMARY OF THERMAL HYDRAULIC VARIABLES [33]

Thermal hydraulic variable	Value	Unit
Pressure vessel	80.78	m^3
Pressurizer	8.078	m^3
Average liquid density	746	kg/m^3
Average steam density	102.8	kg/m^3
Thermal power	150.0	MWth
Generator power	45.0	MWe
pressurizer pressure	15.5	MPa
Steam pressure	2.7	MPa
Cold leg temperature	255.51	$^\circ C$
Average coolant/core temperature	287.5	$^\circ C$
Hot leg temperature	320.36	$^\circ C$
Saturation temperature at 15.5 MPa	344.8	$^\circ C$
Average fuel temperature	849.84	$^\circ C$
Feed water flow	78	kg/s
Coolant flow	424	kg/s
List of safety setpoints		
Safety pressure	<17.05	MPa
Hot leg temperature	<340	$^\circ C$
Peak fuel temperature	<1087.25	$^\circ C$
Maximum neutron flux (p.u. power)	<120	%

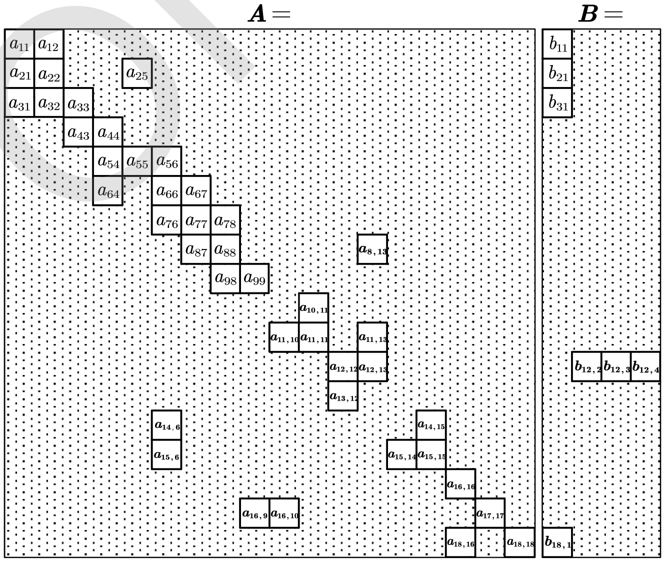

Fig. 5. SMR state-space matrices in coordinate format.

idea AC-DC rectifiers; PGM2: ideal DC power; (2) power distribution: cable sections, and ideal switchboard, ideal DC-AC inverter; (3) load: PCM and PMM [28], [29].

1) Modeling of SM and Interface with SMR: As analyzed in Section II, the SMR generates mechanical power $P_m(t)$ and drives the SM to produce electricity. And then the SM feeds back the rotor speed $w(t)$ to the governor to regulate the output thermal power of SMR, thereby adjusting the output electrical power and frequency at the AC terminal to vary with changes in the load. In terms of modeling SMs, a common approach is to construct equivalent circuits based on the rotor reference frame using controlled current sources or voltage sources [34]. In this paper, the current sources based model is chosen, which results in a 9th-order state-space model, consisting of a 7th-order electrical model and a 2nd-order mechanical model [35], [36]. After discretization using the Trapezoidal method, the per-unit form of SM state-space electrical model is given by:

$$\begin{cases} \hat{\boldsymbol{X}}_{(k+1)} = \boldsymbol{A_d}\hat{\boldsymbol{X}}_{(k)} + \boldsymbol{B_d}\left(\hat{\boldsymbol{U}}_{(k+1)} + \hat{\boldsymbol{U}}_{(k)}\right) \\ \hat{\boldsymbol{Y}}(k+1) = \boldsymbol{I_{SM}} = \mathbb{L}^{-1}\hat{\boldsymbol{X}}(k+1) \\ \boldsymbol{I_{SM}} = \begin{bmatrix}-I_q & -I_d & I_0 & I_{fd} & I_{kd} & I_{kq1} & I_{kq2}\end{bmatrix}^T \\ \hat{\boldsymbol{X}}_{(k)} = \begin{bmatrix}\phi_q & \phi_d & \phi_0 & \phi_{fd} & \phi_{kd} & \phi_{kq1} & \phi_{kq2}\end{bmatrix}^T \\ \hat{\boldsymbol{U}}_{(k)} = \begin{bmatrix}V_q & V_d & V_0 & V_{fd} & 0 & 0 & 0\end{bmatrix}^T \\ \hat{\boldsymbol{A}} = -\left(\mathbb{R} * \mathbb{L}^{-1} + w(k)\right) \\ \boldsymbol{A_d} = \left(\boldsymbol{I}_{7\times7} - w_b\frac{h}{2}\hat{\boldsymbol{A}}\right)^{-1}\left(\boldsymbol{I}_{7\times7} + w_b\frac{h}{2}\hat{\boldsymbol{A}}\right) \\ \boldsymbol{B_d} = w_b\frac{h}{2}\left(\boldsymbol{I}_{7\times7} - w_b\frac{h}{2}\hat{\boldsymbol{A}}\right)^{-1} \end{cases}, \tag{24}$$

where ϕ represents flux, V and I are the voltage and current of

This article has been accepted for publication in IEEE Transactions on Energy Conversion. This is the author's version which has not been fully edited and content may change prior to final publication. Citation information: DOI 10.1109/TEC.2024.3375256

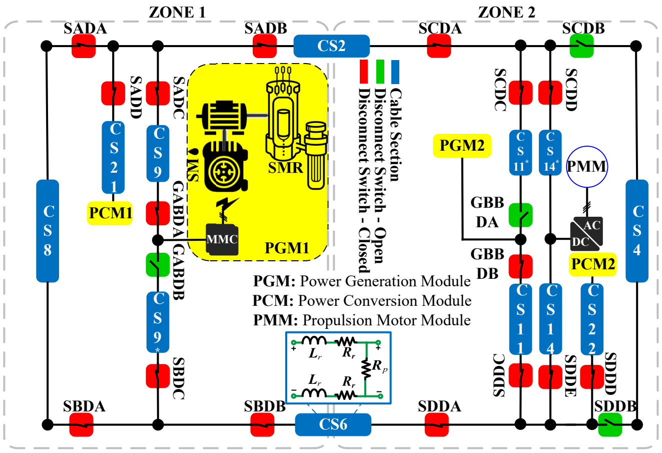

Fig. 6. Modified conceptional two-zone MVDC ship-board power system equipped with SMR.

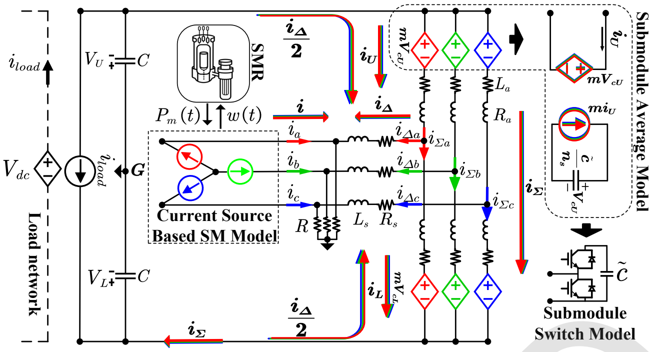

Fig. 7. SMR - SM - MMC integrated transient model.

SM equivalent circuit in the rotor reference frame (dq frame), respectively, $\boldsymbol{I}_{i\times i}$ is an i-dimensional identity matrix, $\mathbb{R}$ and $\mathbb{L}$ are matrices composed of resistances and inductances in the SM, w_b is the rated angular velocity, h is the time interval between $\hat{\boldsymbol{X}}_{(k+1)}$ and $\hat{\boldsymbol{X}}_{(k)}$, and the subscripts d,q and f,k represent d-axis quantity, q-axis quantity, field winding quantity, and damper winding quantity, respectively. The mechanical model contains the interactive variables P_m and w of both SMR and SG, shown as: $\begin{cases} \delta\dot{w} = \frac{\left(\frac{P_m}{w} - T_e - wF\right)}{2\hat{H}} \\ \dot{\theta} = w_b \delta w \end{cases}$, where δw is the rotor speed deviation, θ is the rotor angle, $\hat{H}$ is the inertia coefficient, F is the friction factor, and $T_e = (\phi_d I_q - \phi_q I_d)$ is the electromagnetic torque. Accordingly, based on the θ and inverse Park transformation, three-phase alternating current can be inferred, and thus the controlled-current source model of SM is derived.

2) Modeling of MMC and Interface with SM: The arm-level averaged (ALA) MMC model is utilized, which approximates n_s-submodules MMC arms as ideal coupling dependent $V-I$ sources during the switching period [37]. The SMR-SM-MMC integrated model is given in Fig. 7, where the loading terminal is represented by a controlled current source i_{load}. The selection of MMC state space variables adopts $\Sigma\Delta$-reference frame [38], resulting in $\begin{bmatrix} \mathcal{X}_\Sigma \\ \mathcal{X}_\Delta \end{bmatrix} = \frac{1}{2}\begin{bmatrix} 1 & 1 \\ 1 & -1 \end{bmatrix}\begin{bmatrix} \mathcal{X}_U \\ \mathcal{X}_L \end{bmatrix}$, where U and L refer to the MMC upper and lower arm, respectively, and $\mathcal{X}$ represents arbitrary variables (voltage, current, or modulation input). Illustrating with the example of phase-a current, $i_{\Delta a}$ equals to $\frac{(i_{Ua} - i_{La})}{2}$ and $i_{\Sigma a}$ is $\frac{(i_{Ua} + i_{La})}{2}$. Subsequently, adopting $\Sigma\Delta - \alpha\beta 0-$frame, the state-space form of the ALA MMC can be derived as:

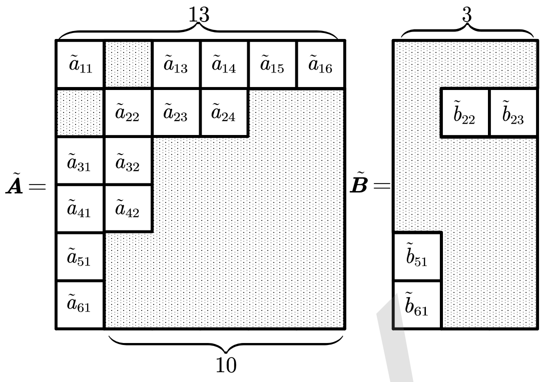

Fig. 8. MMC state space matrices in coordinate format.

$$\begin{cases} \dot{\tilde{\boldsymbol{X}}} = \tilde{\boldsymbol{X}}\tilde{\boldsymbol{A}} + \tilde{\boldsymbol{B}}\tilde{\boldsymbol{U}} \\ \tilde{\boldsymbol{X}} = \begin{bmatrix} \boldsymbol{I}_\Sigma & \boldsymbol{I}_{\boldsymbol{\Delta}} & \boldsymbol{V}_{\boldsymbol{c\Sigma}} & \boldsymbol{V}_{\boldsymbol{c\Delta}} & V_U & V_L \end{bmatrix}^T \\ \tilde{\boldsymbol{Y}} = V_{dc} = \underbrace{\begin{bmatrix} 0 & \cdots & 0 \end{bmatrix}}_{Index\ 1_{st}\sim 11_{th}} \quad -1 \quad -1] \tilde{\boldsymbol{X}} \\ \tilde{\boldsymbol{U}} = \begin{bmatrix} i_{load} & i_\alpha + i_{\Delta\alpha} & i_\beta + i_{\Delta\beta} \end{bmatrix}^T \\ \boldsymbol{I}_{\boldsymbol{\Sigma}} = \begin{bmatrix} i_{\Sigma\alpha} & i_{\Sigma\beta} & i_{\Sigma 0} \end{bmatrix}^T, \boldsymbol{I}_{\boldsymbol{\Delta}} = \begin{bmatrix} i_{\Delta\alpha} & i_{\Delta\beta} \end{bmatrix}^T \\ \boldsymbol{V}_{\boldsymbol{c\Sigma}} = \begin{bmatrix} V_{\Sigma\alpha} & V_{\Sigma\beta} & V_{\Sigma 0} \end{bmatrix}^T, \boldsymbol{V}_{\boldsymbol{c\Delta}} = \begin{bmatrix} V_{c\Delta\alpha} & V_{c\Delta\beta} & V_{c\Delta 0} \end{bmatrix}^T \end{cases}, \tag{25}$$

where sparse matrices $\tilde{\boldsymbol{A}}$ and $\tilde{\boldsymbol{B}}$ are illustrated in Table II and Fig. 8 with a similar COO format to $\boldsymbol{A}$ and $\boldsymbol{B}$. $\mathbb{C}$ is the Clarke transform, $\boldsymbol{V_c}$ is the voltage across each ALA capacitor, n_s is the number of submodules in switched MMC model, i is the SM AC output current, $\boldsymbol{M_{\Sigma/\Delta}}$ is composed of modulation input $m_{\Sigma/\Delta,\alpha\beta 0}$, which respectively represent the modulation signals in the Σ or Δ loop under the $\alpha\beta 0$-frame. Since $\boldsymbol{M}_\Sigma$ and $\boldsymbol{M}_\Delta$ share a similar form, to avoid duplication, the subscript is abbreviated as "Σ/Δ", thus:

$$\begin{cases} \boldsymbol{M}_{\boldsymbol{\Sigma/\Delta}} = \begin{bmatrix} \boldsymbol{M}_{\boldsymbol{\Sigma/\Delta},11} & \boldsymbol{M}_{\boldsymbol{\Sigma/\Delta},12} \\ \boldsymbol{M}_{\boldsymbol{\Sigma/\Delta},21} & m_{\Sigma/\Delta,0} \end{bmatrix} \\ \boldsymbol{M}_{\boldsymbol{\Sigma/\Delta},11} = \begin{bmatrix} \frac{1}{2}m_{\Sigma/\Delta,\alpha} + m_{\Sigma/\Delta,0} & \frac{-1}{2}m_{\Sigma/\Delta,\beta} \\ \frac{-1}{2}m_{\Sigma/\Delta,\beta} & \frac{1}{2}m_{\Sigma/\Delta,\alpha} + m_{\Sigma/\Delta,0} \end{bmatrix} \\ \boldsymbol{M}_{\boldsymbol{\Sigma/\Delta},12} = \begin{bmatrix} m_{\Sigma/\Delta,\alpha} & m_{\Sigma/\Delta,\beta} \end{bmatrix}^T \\ \boldsymbol{M}_{\boldsymbol{\Sigma/\Delta},21} = \begin{bmatrix} \frac{1}{2}m_{\Sigma/\Delta,\alpha} & \frac{1}{2}m_{\Sigma/\Delta,\beta} \end{bmatrix} \\ \mathring{M}_{\boldsymbol{\Sigma/\Delta}} = \begin{bmatrix} \boldsymbol{M}_{\boldsymbol{\Sigma/\Delta},11} & \boldsymbol{M}_{\boldsymbol{\Sigma/\Delta},12} \end{bmatrix} \\ \bar{M}_{\boldsymbol{\Sigma/\Delta}} = \begin{bmatrix} \boldsymbol{M}_{\boldsymbol{\Sigma/\Delta},11} & \boldsymbol{M}_{\boldsymbol{\Sigma/\Delta},21} \end{bmatrix}^T \end{cases}. \tag{26}$$

Based on the above equations, the 13th-order state-space form of the ALA MMC model (neglecting the zero-sequence current $i_{\Delta 0}$) is obtained, where the inputs consist of two parts: one is the DC bus load, which is defined as a controlled current source i_{load}; the other is the input voltage $R(\boldsymbol{i} + \boldsymbol{i_\Delta})$ at the

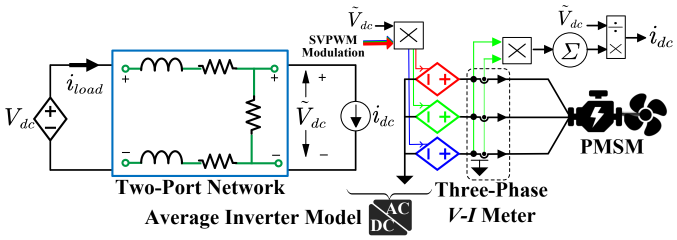

Fig. 9. Power distribution system integrated with PMM.

AC side. The output is the main DC bus voltage, defined as $V_{dc} = -(V_U + V_L)$.

3) Modeling of Power Distribution Networks and Interface with Loads: The power distribution system of two zone MVDC SPS can be simplified as an RL two-port network, as illustrated in Fig. 9, where corresponding PCMs load power and cable impedance data can be found in [28]. The integration among power generation, two-port networks, and loads are decoupled via $V - I$ controlled source method. For PMM, an average-value DC-AC inverter, which transfers power to the permanent magnet synchronous motor (PMSM) based on space vector pulse width modulation (SVPWM), was employed to simplify the calculations of the load port voltage $\tilde{V}_{dc}$ and the current i_{dc}.

IV. Hardware Design, Optimization and Implementation

The algorithms of this design are mainly implemented in C language on Vitis HLS®. The main idea of using HLS is to utilize software-based languages, along with rich software libraries, to develop hardware modules, which significantly accelerate development process and simplify the design. Through HLS function synthesis and interface synthesis, the top-level function is synthesized into a hardware module, which includes a body that implements the module's task and a set of input/output (I/O) ports for exchanging data. Each port has an associated protocol attached to its interface that implements its communication mechanism. The generated packages or intellectual property (IP) cores would be imported in Vivado® design suit software for logic synthesis and then bitstream generation based on hardware-description-language (HDL).

A. Task-level Parallelism

Typically, C functions are executed sequentially, as depicted in the 1st phase of Fig. 10, with equations calculated in a certain order. Equations are computed based IEEE 32-bit floating-point number precision, involving basic arithmetic operations and exponentiation. Taking addition as an example, after synthesis with HLS, a floating-point adder is generated with a 3-cycle latency. In the case of sequential computation, the delay of all equations will be quite cumbersome. Therefore, it is necessary to identify the task parallelism of the algorithm. Evidently, (23), (16), (17), and (13)-F_2 are data-independent, and required parameters and initial values are stored in registers in advance. During each iteration update, these four equations can be safely computed in parallel. Conversely, (12) requires the value of $\rho_{ext}(t)$ as input; (13) also invokes next time-step $\rho(t)$ from (12); (19) needs $F_{1,2}$ and thus must wait for the completion of (13), and its result serves (18) and (15); finally, (15) relies on both $n(t)$ and $n'(t)$. Therefore, due to algorithmic factors, these six equations unavoidably lead to data dependencies and must be executed sequentially. (20) and (18) can be computed concurrently due to the absence of data dependencies. Then, for the next computation period, (23) only depends on (19) and (20). Therefore, iterative calculations can be pipelined, allowing the computation of the next period to start immediately once (20) has been completed, instead of waiting for all equations to be computed within the current period. Up to now, the longest latency path is (23)-(12)-(13).F_1-(19)-(20). Due to the fact that (20) is 18th-order ODE, the numerical solving process will be time-consuming. Therefore, a unit delay of $n(t)$ is introduced to break the data dependency between (19) and (20) for detaching (20) from the longest latency path, as illustrated in the 2nd phase of Fig. 10. The transient time of neutron kinetics is generally around 1ms [39], which is 100 times larger than the sampling rate $10\mu s$.

B. Synthesis Latency and Hardware Resource Utilization

The detailed clock cycles and data flow of the SMR solver are shown in the 3rd phase of Fig. 10, with all tasks and arithmetic units strictly aligned with their corresponding clock positions. The entire solver updates the outputs every 92 clock cycles (clks). Similarly, task-level parallelism and data dependency analysis can be applied to the rest systems, where the variables causing data dependency are $P_m(t)$, $w(t)$, $V_{dc}(t)$, and $iload(t)$, respectively. The latency, resource consumption, and testbench error of each system are shown in the Table IV, where TB represents the testbench. DSPs play a crucial role in enabling high-speed floating-point computations. The SMR solver is found to be the most computationally intensive module due to its high-order equations and multiple summation and exponentiations. The FFs, on the other hand, serve to build registers that store states and intermediate results, and their usage is directly related to the number of variables. In addition, the LUTs are employed to facilitate logical operations. Specifically, in control loops, tasks such as variable gain, hysteresis control, and SVPWM are typically executed through large-scale logic circuits implemented using LUTs. The numerical algorithms and models employed in offline simulation tool Simulink® differed from those used in the hardware emulation (which introduced two extra delays). Therefore, testing is crucial to verify the performance of the HLS-synthesized functions. The testbench data was derived from offline simulation results and compared against HLS. As shown in the table, the error was found to be at the level of one in ten thousand, which is negligible.

C. Hardware Implementation

The hardware set-up is presented in Fig. 11. The IP core of the model generated by HLS was implemented on the Xilinx® Virtex UltraScale+ VCU118 Evaluation Platform (part number: xcvu9p-flga2104-2L-e) in Vivado®. This FPGA board, featuring 6,840 DSPs, 2,364,480 FFs, and 1,182,240

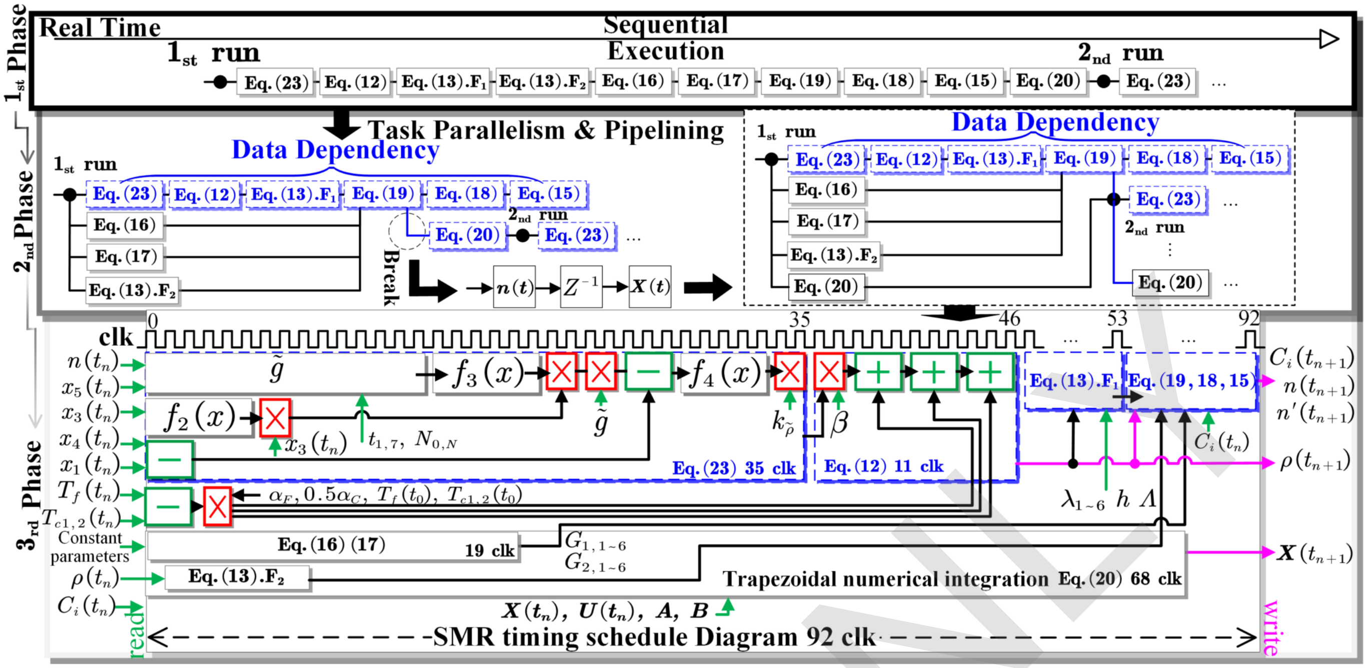

Fig. 10. SMR task-level parallelism solver flowchart for hardware emulation.

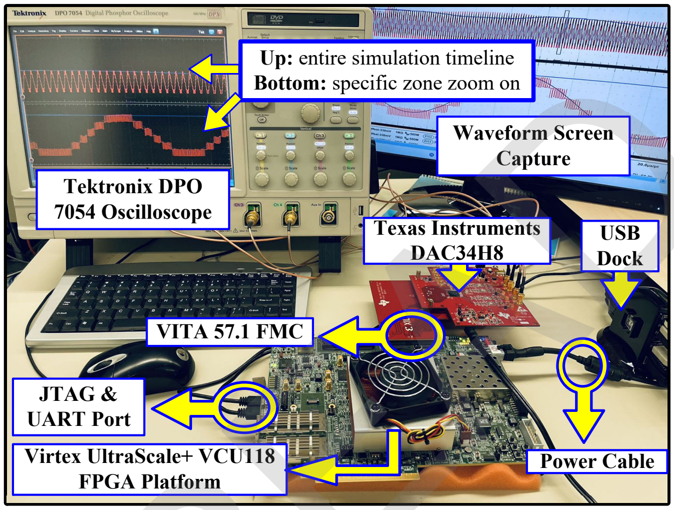
Up: entire simulation timeline
Bottom: specific zone zoom on
Waveform Screen Capture
Tektronix DPO 7054 Oscilloscope
Texas Instruments DAC34H8
USB Dock
VITA 57.1 FMC
JTAG & UART Port
Virtex UltraScale+ VCU118 FPGA Platform
Power Cable

Fig. 11. Real-time hardware emulator for the SMR configured SPS.

TABLE IV
HLS DESIGN SPECIFICS PERFORMANCE

Module	Latency (cycles)	DSP	FF	LUT	TB error
SMR	92	400	37,932	35,697	2.8‱
SM-MMC	162	53	15,142	19,512	3.5‱
RLC-PMM	126	33	5,858	9,050	1.1‱
Total	231 (longest path)	486	58,932	64,259	-

LUTs, supports the complete model implementation without the need for additional hardware, with utilization rates of 7.1%, 2.5%, and 5.4% for DSPs, FFs, and LUTs, respectively. The clock frequency was set to the system clock of 300MHz, with a clock tolerance of 50ppm. Although a user clock with a maximum frequency of 810MHz, is available on this board, it was decided to use the system frequency for the design due to concerns over increased hardware resource consumption and design complexity associated with the higher frequency. Furthermore, the 300MHz (corresponds to a period of approximately 3.33ns) was deemed sufficient to ensure stable operation of real-time emulation. Based on the latency of the longest path in Table IV, it can be estimated that the floating-point arithmetic results are updated every 769.23ns. In order to ensure stable data reception, one cycle buffering was introduced, resulting in a data update time of approximately 800ns. Regarding the I/O, after converting IEEE 32-bit single-precision floating-point numbers to 16-bit signed hexadecimal numbers, data were transmitted to DAC34H8 via the FPGA mezzanine card (FMC) - digital to analog (DAC) adapter in double data rate (DDR) mode, and then display waveforms on the oscilloscope. After configuring the corresponding I/O pins, the bitstream is generated by Vivado on the host computer, and then downloaded to the target FPGA via the USB-JTAG to complete the entire design.

V. EXPERIMENTAL VALIDATION RESULTS

In this paper, the testing scenarios were divided into two categories: offline simulation and real-time emulation. For offline simulation, two scenarios were tested: 1) reactor scram, and 2) SMR integrated with infinite bus system. The purpose of the offline simulation tests is to highlight the superiority of FTRT and emphasize the necessity of (EMT-thermodynamics) multi-domain cosimulation of SMR.

In accordance with the IAEA iPWR specifications [33], during a reactor trip, control rods are inserted into the core at a rate of $80\, steps/min$, completing the insertion within $2s$. The simulation results are illustrated in the Fig. 12. At

This article has been accepted for publication in IEEE Transactions on Energy Conversion. This is the author's version which has not been fully edited and content may change prior to final publication. Citation information: DOI 10.1109/TEC.2024.3375256

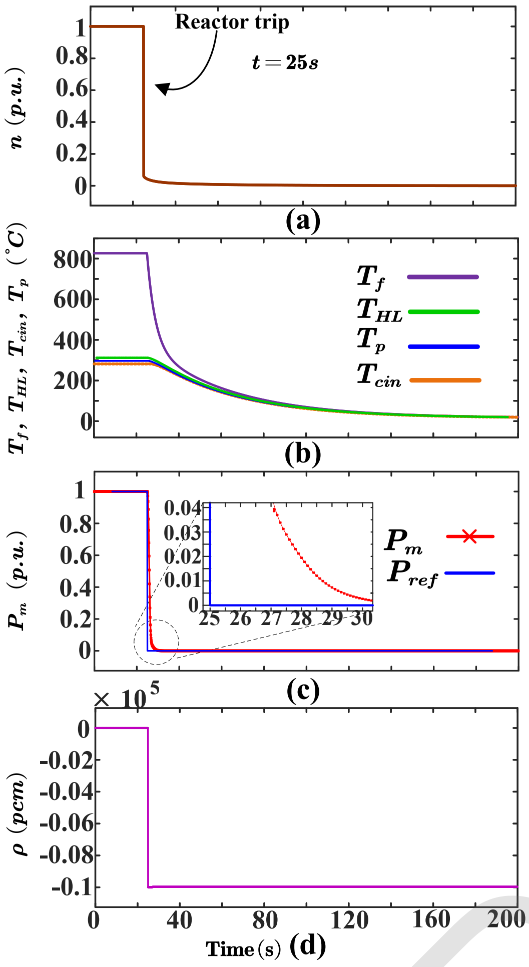

Fig. 12. **Offline simulation results (a)-(d) for the reactor scram**: (a) SMR n. (b) SMR fuel and coolant temperature T_f, T_{HL}, T_{cin}, and T_p. (c) SMR P_m and reference output power P_{ref}. (d) Total core reactivity of SMR ρ.

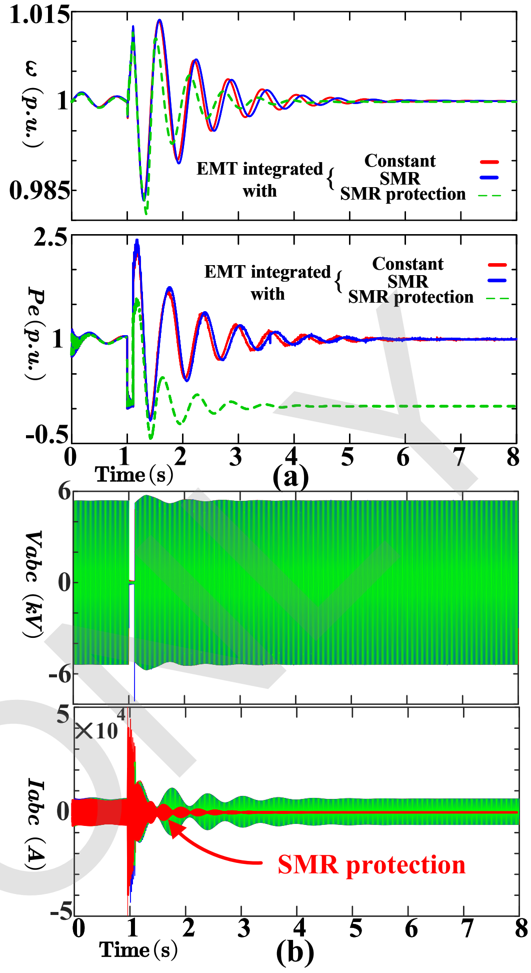

Fig. 14. **Offline simulation results (a)-(b) for SMR integrated with infinite bus short circuit fault**: (a) **Top:** SM speed w; **Bottom:** SM active power P_e. (b) **Top:** AC voltage V_{abc}; **Bottom:** AC current I_{abc}.

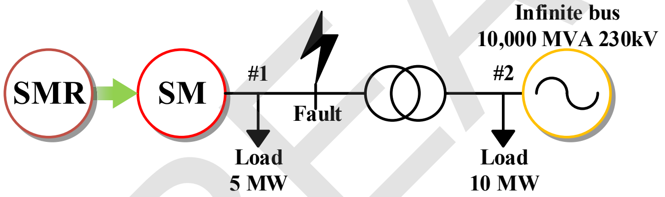

Fig. 13. SMR integrated with infinite bus short circuit fault.

$t = 25s$, the reactor trip was initiated, causing a rapid decrease in the total reactivity ρ within the core to approximately $-10,719\,pcm$. Under these conditions, the generation of neutrons is insufficient to balance neutron losses, and the chain reaction cannot sustain itself, leading to a delayed subcritical state. The neutron density n rapidly decreases, resulting in a decline in thermal power, turbine speed, and zero output mechanical power P_m. Subsequently, n, coolant temperature T_{HL}, T_p, T_{cin}, and core temperature T_f undergo a decay period lasting approximately 200 seconds before reaching a stable state. Similar simulations of SMR operations or malfunctions include scenarios such as main grid power failure, turbine trip, and SG isolation, among others. The steady-state values of various variables during these simulations provide valuable references for engineers in setting setpoints. With a simulation duration of 200 seconds, real-time emulation efficiency is relatively slow. Therefore, if simulations can be conducted at the FTRT speed, it will significantly enhance debugging and experimental efficiency.

For the (EMT-thermodynamics) multi-domain cosimulation of SMR, an illustration involving the SMR integrated with infinite bus short circuit fault is presented, as depicted in Fig. 13. The nominal power, line-to-line voltage, and frequency of the SM are 50MVA, 6.6kV, and 60Hz, respectively. At $t = 1s$, a three-phase short-circuit fault occurs, and the fault is cleared $0.1s$ later. The simulation results are shown in the Fig. 14 and Fig. 15, where Fig. 14 (a) and (b) respectively depict the SM speed w, active power P_e, AC voltage V_{abc}, and current I_{abc}. Specifically, Fig. 14 (a) presents three types of scenarios, namely EMT integrated with: 1) SMR (blue line); 2) SMR terminal as a constant (red line); and 3) SMR with protection mechanism (green dashed line). It can be observed that the first two scenarios have a minor impact on EMT phenomena. This is primarily due to the EMT dynamics having a time

This article has been accepted for publication in IEEE Transactions on Energy Conversion. This is the author's version which has not been fully edited and content may change prior to final publication. Citation information: DOI 10.1109/TEC.2024.3375256

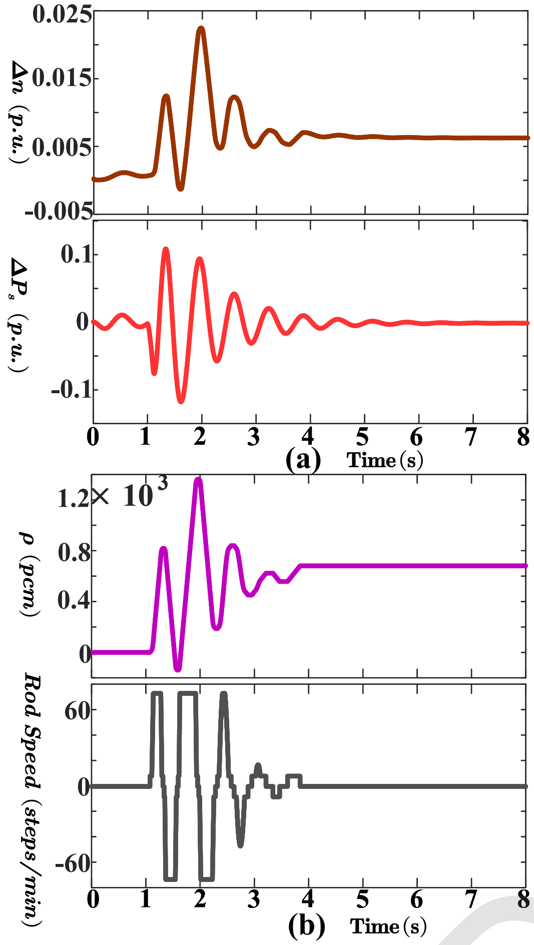

Fig. 15. **Offline simulation results (a)-(b) for SMR integrated with infinite bus short circuit fault**: (a) **Top:** Derivative of SMR n denoted as Δn; **Bottom:** Derivative of SMR P_s denoted as ΔP_s. (b) **Top:** SMR core reactivity ρ; **Bottom:** Control rods speed.

constant much shorter compared to the SMR.

However, EMT phenomena significantly affect the SMR. Fig. 15 (a) reveals that due to fluctuations in the grid frequency, it triggers low-voltage and low-frequency compensation actions in the SMR, causing the SG valve to actuate and resulting in internal pressure fluctuations. At one moment, the pressure surpasses $1.1p.u.$, exceeding the safety margin. In practical engineering, this may trigger protective actions leading to further expansion of the fault at bus No.1, as shown in Fig. 14 (a) and (b). Simultaneously, power mismatch and fluctuations triggered actions in the control system, as shown in Fig. 15 (a) and (b). Within $3s$, signal fluctuations caused a pronounced oscillation in the control rod speed signal within the dead-time control range [33], leading to fluctuations in reactivity ρ and neutron thermal power n. In practical engineering, one of the protective mechanisms for the control rod speed control signal involves designing a filter to eliminate such abrupt fluctuation signals, preventing frequent control rod operations that could pose safety hazards. This highlights the importance of the (EMT-thermodynamics) multi-domain cosimulation of SMR. Subsequently, algorithm validation is conducted through real-time emulation.

The real-time emulation aimed to validate the algorithm's real computational speed, following the Mathwork/Speedgoat® electric ship real-time emulation benchmark [29], with 30s offline simulation time with $h = 10\mu s$, involving full-speed ahead and crash stop operation. This test scenario aims to assess the behavior of the driver during quadrant two regeneration, as depicted in Fig. 16 (i), where a stylized piecewise linear torque-speed curve is illustrated, highlighting an incursion into quadrant two during the crash-stop maneuver. Fig. 16 (a) to (h) present real-time emulation waveform captures on the oscilloscope, where display the entire emulation waveform for one complete cycle and a magnified view of a specific portion in a 1:1 ratio on the upper and lower sub-screens, respectively. Therefore, the emulation time of the upper sub-screen represents the mapping of the 30s offline simulation time, with a 3s/div offline simulation time x-axis scale. To avoid ambiguity and maintain conciseness, the term 'time' used hereafter refers to offline simulation time.

The states of switchboards are illustrated in the Fig. 6, where PGM1 and PGM2 provides power to PMM through the CS9-CS2-CS14* path and CS11-CS14 path, respectively. During initialization the SMR is assumed to operate at rated power, and then the simulation begins. During the time interval $0 \sim 5s$, the ship remains stationary, resulting in almost zero power consumption. In Fig. 16, it can be observed that for approximately the first $1.8s$, due to the larger thermal time constant and the presence of hysteresis control, there is little variation in ρ, n, and temperature. The reactor output power is regulated by the turbine, and as y rapidly decreases, P_m also decreases. Meanwhile, P_s increases since the thermal power remains nearly unchanged. Subsequently, the SMR controller takes action, introducing negative ρ and causing a rapid decrease in n. As a result, the fuel temperature decreases while the coolant temperature rises. Due to the inherent islanding nature, the system is operated based on the droop control and powered by PGM1 and PGM2. As a result, the output power of the SM in PGM1 decreases, and the frequency of the AC portion increases to approximately 1.076 per unit. At $5 \sim 15s$, from Fig. 16 (e) and (f), it can observed that the ship accelerates to 1800rpm and maintains stability. The vector control effectively enables N_{PMSM} to track the reference speed N_{ref}. The P_e increases to 0.45 of the rated power, while the AC frequency decreases and eventually stabilizes at approximately 1.05 of the rated frequency. Although there is some lag in the turbine's mechanical power output, it still manages to stably follow the SM's demand. As a result, ρ increases, leading to an increase in n and a decrease in P_s. According to the design, the droop ratio between PGM1 and PGM2 is 2:1. As can be seen from Fig. 16 (d), PL_2 provides approximately twice the power compared to PL_1, and the combined power of both can stably meet the power requirements of the load. At $15 \sim 30s$, the ship performs a crash stop maneuver. During approximately $18 \sim 20s$, the driver operates in the second quadrant. By examining the zoomed-in subscreen in Fig. 16 (d), the motor is observed to consume negative power, indicating regeneration. This confirms that the design functions correctly. For SMR dynamics, during the forward

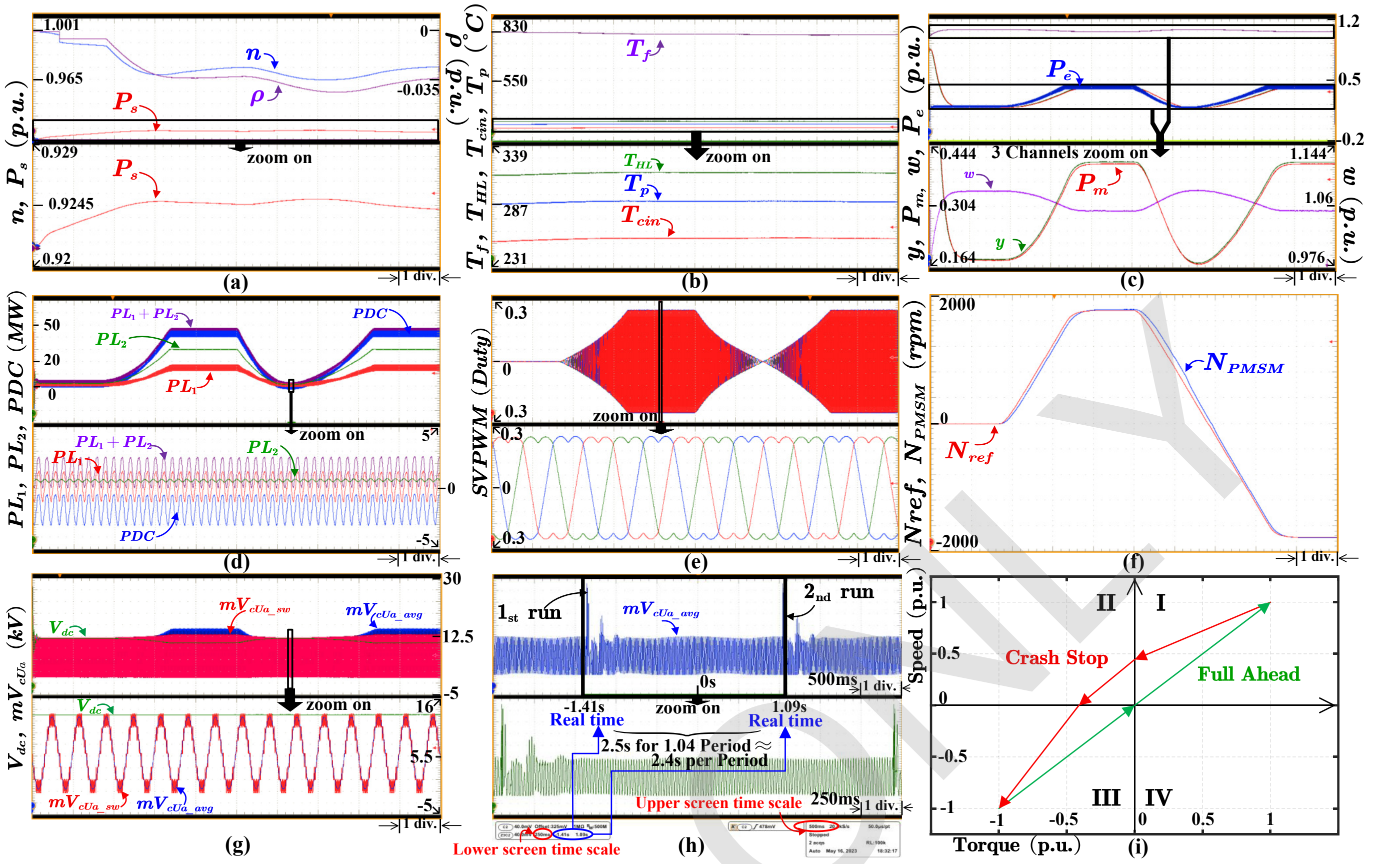

Fig. 16. **Real-time emulation oscilloscope results (a)-(h) with entire emulation period (top) and zoomed-in view (bottom)**: (a) SMR n, ρ, P_s. (b) SMR fuel and coolant temperature T_f, T_{HL}, T_{cin}, and T_p. (c) SMR y, P_m, SM w, and active power P_e. (d) PMSM power PDC, PGM1 DC power PL_1, and PGM2 DC power PL_2. (e) PMSM SVPWM. (f) PMSM speed N_{PMSM} and reference speed N_{ref}. (g) SM-MMC V_{dc}, a-phase upper arm voltage mV_{cUa_age} (average-model), and mV_{cUa_sw} (switch-model). (h) FTRT emulation. (i) Test scenarios. **Real-time x-axis scale: Top:** (a)-(g): 240ms/div; (h): 500ms/div; **Bottom:** (a)(b)(c): 240ms/div; (e): 1.2ms/div; (g)(d): 2.4ms/div; (h): 250ms/div. **Real-time span of oscilloscope capture: Top:** (a)-(g): 2.4s; (h): 5s; **Bottom:** (a)(b)(c): 2.4s; (e): 12ms; (g)(d): 24ms; (h): 2.5s.

deceleration stage, as PDC and P_m diminish, the valve y opening contracts, leading to a reduction in steam outflow. This decrease in steam outflow contributes to an elevation in internal pressure P_s, consequently causing a decline in the output thermal power n. In the reverse acceleration stage, as PDC and P_m escalate, the opening of the valve y enlarges, contributing to a decrease in internal pressure P_s, subsequently leading to an augmentation in n. In the steady-state operation stage, PDC, P_m, and y remain constant. Due to the larger time inertia constant, P_s and n exhibit a stable trend. During the entire full-speed/crash-stop period, the presence of average coolant temperature control ensures minimal fluctuations in the temperature T_f, T_{HL}, T_p, and T_{cin}. Lastly, in Fig. 16 (g), it can be noted that the DC bus voltage fluctuates around 12kV to 10.5kV. The subfigure below demonstrates the excellent alignment of the MMC a-phase upper bridge arm voltage between the switch-model and average-model.

Since the offline simulation time is 30s with $h = 10\mu s$, it can be calculated that 3 million calculations are needed to obtain the entire simulation waveform. Next, the validation of the emulation time used proceeds, where all the mentioned 'time' refer to real-time. Fig. 16 (h) demonstrates the actual operation time and scale, with the lower subscreen showing the time interval between two operating cycles, approximately 2.4s. Considering the calculation Latency of this design, each data update takes approximately 800ns, and the total calculation time of 3 million iterations amounts to about 2.4s. Thus, it can be confirmed that this design achieves approximately 12.5 times FTRT acceleration ratio.

VI. Conclusion

This paper proposed a hardware emulation solution for the SMR based SPS technology, achieving a 12.5-fold FTRT acceleration ratio. A semi-analytical method for solving the point-reactor neutron-kinetics model was proposed, addressing the challenge of numerical stiffness. Besides, a detailed multi-domain modeling of the entire SMR was developed, including an 18th order mathematical model. Additionally, real-time operation, optimization, and acceleration schemes for the model were meticulously designed, and the hardware synthesis and implementation processes were thoroughly discussed. The open-source Speedgoat® real-time emulation template for two-zone MVDC ship was selected and modified as the test case, with the model and algorithms deployed on the Xilinx® VCU 118 FPGA board. Ultimately, under the 30s offline simulation with $10\mu s$ time-step, the 800ns real-time data update interval was achieved, completing the entire real-time emulation in approximately 2.4s, yielding a 12.5 times FTRT acceleration ratio. These achievements demonstrate the effectiveness and efficiency of the proposed methodology and its practical applicability to real-time emulation of SMR systems, providing valuable insights and practical solutions for nuclear related EMT studies.

REFERENCES

[1] Advance in SMR technology development. Vienna: IAEA, 2020. [Online]. Available: https://aris.iaea.org/Publications/SMR_Book_2020.pdf

[2] T. Ichikawa and T. Inoue, "Light water reactor plant modeling for power system dynamics simulation," *IEEE Trans. Power Syst.,* vol. 3, no. 2, pp. 463-471, May. 1988.

[3] Z. Dong, "Model-free power-level control of MHTGRs against input saturation and dead-zone," *IEEE Trans. Nucl. Sci.*, vol. 62, no. 6, pp. 3297-3310, Dec. 2015.

[4] B. Poudel and R. Gokaraju, "Small Modular Reactor (SMR) Based Hybrid Energy System for Electricity & District Heating," *IEEE Trans. Energy Convers.,* vol. 36, no. 4, pp. 2794-2802, Dec. 2021.

[5] T. W. Kerlin and E. M. Katz, "Pressurized-water-reactor modeling for long-term power-system-dynamics simulations," *Final report (No. EPRI-EL–3087-VOL. 2),* Tennessee Univ., 1983.

[6] M. S. Di Lascio, R. Moret, and M. Poloujadoff, "Reduction of program size for long-term power system simulation with pressurized water reactor," *IEEE Power Eng. Rev.,* vol. PER-3, no. 3, pp. 43-43, Mar. 1983.

[7] J. J. Duderstadt and L. J. Hamilton, *Nuclear Reactor Analysis,* New York, NY, USA: Wiley, pp. 233-556, 1976.

[8] D. Bose, S. Banerjee, M. Kumar, P. P. Marathe, S. Mukhopadhyay, and A. Gupta, "An interval approach to nonlinear controller design for load-following operation of a small modular pressurized water reactor," *IEEE Trans. Nucl. Sci.,* vol. 64, no. 9, pp. 2474-2488, Sep. 2017.

[9] B. Puchalski, T. A. Rutkowski, and K. Duzinkiewicz, "Nodal models of pressurized water reactor core for control purposes - comparison study," *Nucl. Eng. Des.,* vol. 322, pp. 444-463, 2017.

[10] B. Poudel, K. Joshi, and R. Gokaraju, "A dynamic model of small modular reactor based nuclear plant for power system studies," *IEEE Trans. Energy Convers.,* vol. 35, no. 2, pp. 977-985, Jun. 2020.

[11] A. Sabir, D. Michaelson, and J. Jiang, "Load-frequency control with multimodule small modular reactor configuration: modeling and dynamic analysis," *IEEE Trans. Nucl. Sci.,* vol. 68, no. 7, pp. 1367-1380, Jul. 2021.

[12] Instrumentation and control systems for advanced small modular reactors. Vienna: IAEA, 2017. [Online]. Available: https://www-pub.iaea.org/MTCD/publications/PDF/P1770_web.pdf

[13] B. Poudel and R. Gokaraju, "Small modular reactor (SMR) based hybrid energy system for electricity & district heating," *IEEE Trans. Energy Convers.,* vol. 36, no. 4, pp. 2794-2802, Dec. 2021.

[14] V. Vajpayee, E. Top, and VM. Becerra, "Analysis of transient interactions between a PWR nuclear power plant and a faulted electricity grid," *Energies,* vol. 14, no. 6, pp. 1573, Mar. 2021;

[15] S. Yamoah, E. H. Akaho, and B. J. Nyarko, "An accurate solution of point reactor neutron kinetics equations of multi-group of delayed neutrons," *Ann. Nucl. Energy,* vol. 54, pp. 104-8, Apr. 2013.

[16] A. A. Nahla, "Analytical solution to solve the point reactor kinetics equations," *Nucl. Eng. Des.,* vol. 240, no. 6, pp. 1622-9, Jun. 2010.

[17] W. Chen, J. Hao, L. Chen, and H. Li, "Solution of point reactor neutron kinetics equations with temperature feedback by singularly perturbed method," *Sci. Technol. Nucl.,* Jan. 2013.

[18] MW. da Silva, R. Vasques, BE. Bodmann, and MT. Vilhena, "A nonstiff solution for the stochastic neutron point kinetics equations," *Ann. Nucl. Energy,* vol. 97, pp. 47-52, Nov. 2016.

[19] H. Li, W. Chen, L. Luo, and Q. Zhu, "A new integral method for solving the point reactor neutron kinetics equations," *Ann. Nucl. Energy,* vol. 36, no. 4, pp. 427-32, May 2009.

[20] A. A. Nahla, "Taylor's series method for solving the nonlinear point kinetics equations," *Nucl. Eng. Des.,* vol. 241, no. 5, pp. 1592-5, May 2011.

[21] Z. Zlatev, K. Georgiev, and I Dimov, "Studying absolute stability properties of the Richardson Extrapolation combined with explicit Runge-Kutta methods," *Comput. Math. with Appl.,* vol. 67, no. 12, pp. 2294-307, Jul. 2014.

[22] D. Juszczuk, J. Tarnawski, T. Karla, and K. Duzinkiewicz, "Real-time basic principles nuclear reactor simulator based on client-server network architecture with WebBrowser as user interface," *Proc. of KKA 2017—The 19th Polish Control Conf.,* pp. 344-353, Jun. 2017.

[23] D. J. Rankin and J. Jiang, "A hardware-in-the-loop simulation platform for the verification and validation of safety control systems," *IEEE Trans. Nucl. Sci.,* vol. 58, no. 2, pp. 468-478, Apr. 2011.

[24] Solutions for cost effective assessment of software based instrumentation and control systems in nuclear power plants. ser. TECDOC, no. 1328, IAEA, Dec. 2002. [Online]. Available: https://www.iaea.org/publications/6607/solutions-for-cost-effective-assessment-of-software-based-instrumentation-and-control-systems-in-nuclear-power-plants

[25] S. Cao, N. Lin and V. Dinavahi, "Faster-than-real-time hardware emulation of extensive contingencies for dynamic security analysis of large-scale integrated AC/DC grid," *IEEE Trans. Power Syst.,* vol. 38, no. 1, pp. 861-871, Jan. 2023.

[26] X. Liu, J. Ospina, I. Zografopoulos, A. Russel, and C. Konstantinou, "Faster than real-time simulation: methods, tools, and applications," *Proc. of the 9th Workshop on Modeling and Simulation of Cyber-Physical Energy Syst.,* pp. 1-7. May 2021.

[27] V. Dinavahi and N. Lin, *Real-Time Electromagnetic Transient Simulation of AC-DC Networks*, Wiley-IEEE Press: New Jersey, USA, 2021.

[28] "Documentation for a notional two zone medium voltage DC shipboard power system model implemented on the RTDS." Dec. 2016. [Online]. Available: https://www.esrdc.com/library/documentation-for-a-notional-two-zone-medium-voltage-dc-shipboard-power-system-model-implemented-on-the-rtds/

[29] "Shipboard power system in Simscape." Dec. 2022. [Online]. Available: https://www.mathworks.com/matlabcentral/fileexchange/76995-shipboard-power-system-in-simscape

[30] W. Chen, T. Liang, and V. Dinavahi, "Comprehensive real-time hardware-in-the-loop transient emulation of MVDC power distribution system on nuclear submarine," *IEEE open j. Ind. Electron. Soc.,* vol. 1, pp. 326-339, Nov. 2020.

[31] "Solver that computes states and outputs for simulation." Mar. 2023. [Online]. Available: https://www.mathworks.com/help/simulink/gui/solver.html?searchHighlight=solver&s_tid=srchtitle_solver_2

[32] A. Marciniak, "A resume on interval Runge-Kutta methods," *Math. Appl.,* Vol. 40, pp. 1-1, Aug. 2012.

[33] C. Batra, *Integral Pressurized Water Reactor Simulator Manual,* International Atomic Energy Agency, Vienna, Austria, vol. 1, 2018.

[34] L. Wang, J. Jatskevich, C. Wang, and P. Li, "A voltage-behind-reactance induction machine model for the EMTP-type solution," *IEEE Trans. Power Syst.,* vol. 23, no. 3, pp. 1226-1238, Aug. 2008.

[35] S. Cao, N. Lin, and V. Dinavahi, "Faster-than-real-time dynamic simulation of AC/DC grids on reconfigurable hardware," *IEEE Trans. Power Syst.,* vol. 35, no. 2, pp. 1539-1548, Mar. 2020.

[36] P. Kundur, *Power System Stability and Control,* New York, McGraw-Hill, 1994.

[37] K. Sun, D. Soto, M. Steurer, and M. O. Faruque, "Experimental verification of limiting fault currents in MVDC systems by using modular multilevel converters," *IEEE Electric Ship Technologies Symposium (ESTS)*, Old Town Alexandria, VA, USA, pp. 27-33, Jun. 2015.

[38] G. Bergna-Diaz, J. Freytes, X. Guillaud, S. D'Arco, and J. A. Suul, "Generalized voltage-based state-space modeling of modular multilevel converters with constant equilibrium in steady state," *IEEE J. Emerg. Sel. Top. Power Electron.,* vol. 6, no. 2, pp. 707-725, Jun. 2018.

[39] T. W. Kerlin, and B. R. Upadhyaya, *Dynamics and control of nuclear reactors,* 1st ed. San Diego, CA, USA: Academic, 2019.

Weiran Chen (Student Member, IEEE) received the B.Eng. degree in electrical engineering from Harbin Engineering University, Harbin, Heilongjiang, China, in 2018. He is currently pursuing the Ph.D. degree in electrical and computer engineering at the University of Alberta, Edmonton, AB, Canada. His research interests include real-time simulation of power systems, power electronic systems, and field programmable gate arrays.

This article has been accepted for publication in IEEE Transactions on Energy Conversion. This is the author's version which has not been fully edited and content may change prior to final publication. Citation information: DOI 10.1109/TEC.2024.3375256

Venkata Dinavahi (Fellow, IEEE) received the B.Eng. degree in electrical engineering from Visvesvaraya National Institute of Technology (VNIT), Nagpur, India, in 1993, the M.Tech. degree in electrical engineering from the Indian Institute of Technology (IIT) Kanpur, India, in 1996, and the Ph.D. degree in electrical and computer engineering from the University of Toronto, Ontario, Canada, in 2000. He is currently a Professor with the Department of Electrical and Computer Engineering, University of Alberta, Edmonton, Alberta, Canada. He is a Fellow of the Engineering Institute of Canada (EIC) and a Fellow of the Asia-Pacific Artificial Intelligence Association (AAIA). His research interests include real-time simulation of power systems and power electronic systems, electromagnetic transients, device-level modeling, artificial intelligence machine learning, large-scale systems, and parallel and distributed computing.

Ning Lin (Member, IEEE) received the B.Sc. degree in applied electronics engineering and M.Sc. degree in electrical engineering from Zhejiang University, Hangzhou, China, in 2008 and 2011, respectively, and the Ph.D. degree in energy systems from the University of Alberta, Edmonton, AB, Canada, in 2018. From 2011 to 2014, he was an Engineer in substation automation, FACTS, and HVdc control and protection. He is currently a Senior Power Systems Consultant at Powertech Labs Inc. His research interests include AC/DC grids, electromagnetic transient simulation, hardware emulation, power system stability analysis, and heterogeneous high-performance computing of power electronics and power systems on GPU.